Meccanica (2025) 60:1601–1612
https://doi.org/10.1007/s11012-024-01844-9

RESEARCH

Sensitivity to entrance conditions of wall shear stress in a curved vessel

Yuling Chen · Xavier Escriva · Thomas Castelain · Patrick Feugier · Bruno Gilles · Jean-Christophe Béra

Received: 28 February 2024 / Accepted: 19 June 2024 / Published online: 4 August 2024

Abstract This study aims to numerically investigate the impact of entrance velocity distributions on wall shear stress in a simplified curved vessel model. The flow in a single-curved vessel is simulated with Reynolds numbers adjusted to a Newtonian blood-analog fluid in an external iliac artery (EIA) model. Simulations are conducted assuming a rigid wall and a steady-state flow regime using OpenFOAM®. Eight entry velocity conditions are implemented, including the effects of flow development, asymmetry, Dean-type secondary flow and rotation. Their influences on hemodynamics features are investigated, focusing on axial wall shear stress (WSS). In the examined configurations of EIA flow, the impact of entrance conditions on WSS distribution is moderate. The maximum WSS is consistently located at the bend exit on the outer wall, except in the case mimicking an upstream curved pipe in the opposite direction of the local curvature. While the entry condition affects the maximum WSS value, this value remains within the same order of magnitude. At $Re = 560$, the highest WSS value is given by the *Poiseuille* condition and reaches 4.9 times the value of the laminar straight flow. At $Re = 1100$, the maximum value provided by the Dean-type condition, particularly in the case mimicking an upstream curved pipe perpendicular to the local curvature, reaching 7.1 times the laminar straight flow, which exceeds the value of the *Poiseuille* condition by 17%. The results suggest that, to capture extreme WSS value, opting for *Poiseuille* flow as the entrance condition is a good choice for further studies on EIA flow. It has to be noted that results presented here tend to confirm the link established between exaggerated WSS and the endofibrosic plaque development.

Keywords Wall shear stress · Curved pipe · Vascular flow · Entrance condition · External iliac endofibrosis

Y. Chen · X. Escriva · T. Castelain · P. Feugier
LMFA, UMR5509, CNRS, INSA Lyon, Universite Claude Bernard Lyon 1, Ecole Centrale de Lyon, 69622 Villeurbanne, France

Y. Chen (✉) · B. Gilles · J.-C. Béra
LabTAU, INSERM, Centre Léon Bérard, Université Lyon 1, 69003 Lyon, France
e-mail: yuling.chen@inserm.fr

P. Feugier
Hôpital Lyon Sud, Hospices Civils de Lyon, Lyon, France

1 Introduction

Atherosclerosis is associated with several well-identified risk factors (i.e., diabetes mellitus, tobacco abuse, hypercholesterolemia, hypertension [1]). Evidence has shown, mainly from studies primarily focused on large arteries, such as the carotid bifurcation [2] and the coronary arteries [3], that low wall shear stress (WSS) is associated with the development of atherosclerotic plaques [4–6]. On the other hand, due to

its low prevalence, only few studies can be found on non-atherosclerotic peripheral artery disease, such as fibromuscular dysplasia, intimal hyperplasia and external iliac artery endofibrosis (EIAE) [7]. Moreover, these studies have shown that non-atherosclerosis is not related to classical cardiovascular risk factors [8] and it is rather high WSS that may be the trigger for artery obstruction [9].

In particular, EIAE is a non-atheromatous vascular pathology specific to athletes, such as cyclists, rowers, and ultra-trail runners. It is defined histologically by an intimal fibrosis leading to the wall thickening and the reduction of the iliac artery lumen caliber [10]. Numerous etiological hypotheses have been proposed to explain the pathological development but no dedicated study has yet tested these hypotheses on in vitro, in vivo or in silico experiments. Several authors have proposed that the locally exaggerated WSS is a leading etiological factor [11–13]. Moreover, regions of high WSS gradients (WSSG) have been associated with intimal hyperplasia [9], whose histopathological description and potential etiopathogenic mechanism closely correlate with EIAE [14]. The knowledge of WSS and WSSG distributions in iliac artery model is a key to understand the development of EIAE. WSS can be determined by a conjunction of flow rate, geometry and entrance condition. It is noteworthy that the majority of EIAE patients exhibit an excessive length of the iliac artery, leading to arterial over-curvature and complicating the upstream flow [15]. The flow entrance condition in the curved portion could be important because of its potential contribution to determine the sites of WSS extreme value [16]. The present work specifically addresses the issue of the influence of entrance conditions on the WSS distribution in a model of curved artery.

The body of research on entry condition began in 1974 with Singh [17], who reported that the nature of the entry condition appreciably influences the initial development of the curved pipe flow, by analysing steady flow under both constant dynamic pressure and uniform velocity conditions. Later, the effect of uniform entry velocity on the pressure drop and production of vortex structures has been of broad interest experimentally [18] and numerically [19, 20] in curved circular pipe.

Compared to the flow in a straight pipe, the flow in a curved pipe of same length has more pressure losses [21] and shorter distance to become fully developed [22]. Williams et al. [23] conducted experiments providing the initial observations on curved pipe flow, he observed that the maximum axial velocity occurs near the outer side of the pipe, next to the boundary layer.

Dean [24] was the first to show mathematically the existence of one pair of counter-rotating vortices for the fully developed viscous flow of a Newtonian fluid in a curved pipe. He characterized the flow in curved pipes by considering it as a perturbation of Poiseuille flow. In Dean's equation for a loosely curved pipe flow, whose curvature ratio $\delta << 1$ ($\delta = \frac{D}{2R_c}$, where R_c is the curvature radius and D is the pipe diameter), the only parameter that characterizes the flow is the Dean number. According to different authors [24, 25], this dimensionless quantity can be defined as:

$$Dn = 2\sqrt{2}Re\sqrt{\delta}$$

where Re is the Reynolds number. The Dean number serves as a crucial metric quantifying the secondary flow magnitude. It is related to the product of inertia and centrifugal forces, dividing by the viscous force. The secondary flow is found to be very appreciable beyond a threshold ($Dn = 600$) [25]. The Dean numbers treated in this work, $Dn = 650$ and $Dn = 1273$, fall within the range of large Dean numbers. The chosen Reynolds numbers are $Re = 560$ and $Re = 1100$, corresponding to resting and moderate exercise conditions in human iliac artery, as measured by Ku [26] in an experimental study of a steady Newtonian flow in a rigid glass model of the human abdominal artery.

Eustice et al. [27] employed dyeing techniques to experimentally validate the existence of cross-sectional flow in a curved pipe, generated by the centrifugal force due to the bend itself. Alastruey et al. [28] showed that cross-sectional flow motions directly affect the radial displacement of the peak axial velocity, and alternate the position of the maximum velocity between the inner and outer cores. This cross-sectional flow motion is typically an order of magnitude smaller than the axial flow, and is difficult to be measured with reasonable accuracy and reproducibility. However, its influences on flow dynamics have been found to be significant [29–33]. A numerical study in the carotid bifurcation concluded that entry conditions with secondary flow produce less changes in WSS distribution compared to those caused by local curvature [3]. However, their study only examined

small secondary flow (Dn=102). Building upon their research, our study aims to further explore the influence of entry flow with secondary components of large Dean numbers. Caro et al. [34] observed human artery imaged by magnetic resonance angiography and supposed that losing straightness in arteries may lead to asymmetry in the velocity field. This observation motivated the current work to study the effect of off-center asymmetric *Poiseuille* profile at the entrance on WSS distribution.

While many studies use patient-specific geometries to study blood flow of peripheral arterial diseases, another approach consists in adopting idealized model to grasp the underlying flow physics without the added complexity of variable geometry, such as branches and stenosis. Following the latter approach, the present work consists of a numerical investigation of a simplified artery model, assuming the vessel curvature as the predominant cause of excessive WSS. Hemodynamic parameters such as non-Newtonian fluid behavior, wall elasticity or pulsatility (Womersley number Wo in the external iliac artery reaches 5.5 [35]), can play significant roles in arterial flows. Several studies have investigated the effects of these parameters on WSS. Ku's experimental study [36] on peripheral artery flow (Re=250, Wo =2.3) measured the maximum shear gradient values under both Newtonian and non-Newtonian models. For rigid wall conditions, values of 1400 and 1100 s^{-1} were respectively obtained. Regarding wall elasticity effects, due to fluid inertia, the curvature radius undergoes a local increase in the case of an elastic wall, which can lead to a reduction in wall shear stress, compared to rigid wall models. Nevertheless, Pielhop et al. [37] showed that in a configuration with vessel dilation as high as 6% and a Reynolds number between 300 and 1000, as fbased on an O-grid structuredlong as $Wo < 6$, the bias of the WSS keeps of the order of 10%. Considering the moderate effects of these parameters on shear gradients, this preliminary study focuses on Newtonian and rigid wall models. For pulsatility effects, the situation is different, since large WSS bias can be obtained for Womersley number of about 6 [38]. However, the external iliac flow configuration studied here corresponds to a not fully developed Dean flow for which very few results can be found in the literature. For that reason, the present study focuses on steady-state flows, in order to provide reference values for further comparative studies on unsteady flows at moderate Wo. Moreover, as opposed to curvature effects, it has to be noted that none of those effects involve any aspect specific to the development of EIAE.

Four specific inlet conditions are examined using the finite volume-based open-source software OpenFOAM®: (1) an axisymmetric *Poiseuille* flow; (2) a profile featuring a uniform inlet flow; (3) an asymmetric laminar profile whose maximum velocity is off-center, considering the geometric complexity in human arteries; and (4) a profile which incorporates a cross-sectional flow of large Dean number, mimicking an upstream curved pipe as a more realistic condition. For the latter two non-axisymmetric conditions, three orientations of the entrance flow about the local curvature direction are also considered.

2 Methods

2.1 Artery model and flow condition

A simplified artery model is adopted considering fixed geometry with a rigid-wall circular pipe of diameter D, containing a single-curved portion characterized by a curvature radius R_c and an angular aperture θ_{max}. The geometric parameters chosen are derived from MRI image analysis conducted on five patients experiencing EIAE localized to one leg. The affected region, identified through a reduction in diameter, exhibits a distinctive curvature compared to the corresponding area in the healthy leg. The parameter values selected for this study from the average values of the five patients are: $R_c = 3D$ and $\theta_{max} = 55°$.

A straight $3.5D$ length section is added upstream of the curvature entrance, as well as another $10.5D$ straight section, downstream from the curvature exit as shown in Fig. 1. Any cross section along the pipe is localized by the curvilinear abscissa along the centerline s, varying from $-6.3D$ to $10.5D$, the bend entrance corresponding to $s = -2.9D$ ($\theta = 0$) and the bend exit to $s = 0$ ($\theta = \theta_{max}$).

The Reynolds number is defined as $Re = \frac{\bar{U}D}{\nu}$, with a fixed curvature ratio $\frac{D}{2R_c} = \frac{1}{6}$, $\bar{U}$ being the mean velocity and ν the kinematic viscosity. Considering physiological flow conditions in human iliac artery, provided by Ku [26], two Re values are studied:

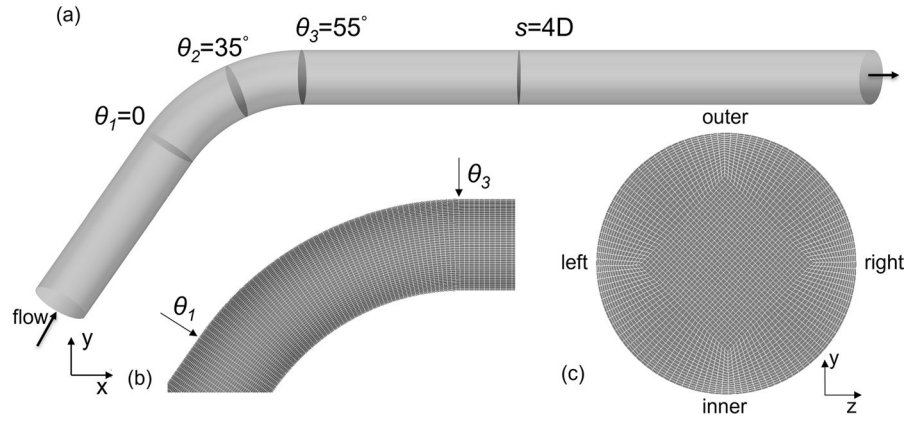

Fig. 1 Simplified curved artery geometry and orientation: **a** curved pipe with flow direction and various cross sections, **b** curvature mesh with connection to upstream and downstream (partial), **c** cross section *yz* plane viewed from upstream

Table 1 Flow conditions

Parameters	Resting	Exercise
R_e	560 [26]	1100 [26]
D_n	230	450
$\bar{U}$ (m/s)	0.056	0.11
Q_v (l/min)	0.265	0.473

$Re = 560$ and $Re = 1100$, corresponding to resting and moderate exercise conditions. Parameter values are given in Table 1, $\bar{U}$ and Q_v values are obtained from Re using a Newtonian blood-analog model with a kinematic viscosity $\nu = 3.8 \times 10^{-6}\, m^2/s$ and a fluid density of $\rho = 10^3\, kg/m^3$.

2.2 Numerical discretisation

The governing equations for a Newtonian and incompressible fluid through a curved pipe in steady-state and laminar regime are the continuity and momentum equations: $\nabla \cdot \mathbf{U} = 0$; $\nabla \cdot \nabla \mathbf{U} = -\nabla p + \nabla \cdot \mathbf{R}$; where $\mathbf{U}$ is the velocity vector, p the kinematic pressure and $\mathbf{R}$ the viscous stress tensor.

Simulations are performed with the finite volume-based OpenFOAM® toolbox, employing the SIMPLE algorithm for coupling the velocity and pressure fields. For spatial derivatives, the discretization of both convective and diffusive transport terms is achieved using the second-order central differencing scheme.

The mesh is based on an O-grid structured pattern in the cross-section of the geometry, with additional refinement near the curved section to ensure equivalent mesh fineness in the upstream and downstream sections compared to the curved section. Figure 1c shows the grid arrangement in the *yz* plane. The cross-sectional area is meshed by 3060 cells, with an inner block size ratio of $\frac{2R_{block}}{D} = 0.67$. The first wall-normal node normalized height, $\Delta y^+ = \frac{\Delta y \bar{U}}{\nu}$, is 3.29. The cell face length in the axial direction is $\Delta s^+ = 20.25$, and $\Delta \phi^+ = 14.26$ in the circumferential direction. The streamwise-to-spanwise grid cell ratio is $\frac{\Delta s^+}{\Delta \phi^+} = 1.42$. The resulting final hexahedral mesh, after a thorough mesh convergence study at R_e=2000 under fully developed inlet condition with an adequate convergence criterion (*residualControl* set to 10^5), comprises 612,000 cells.

The simulation model was first validated comparing to experimental results on velocity contours from Enayet et al. [39], obtained in a configuration corresponding to a 90° bend with a diameter of 48 mm at $Re = 500$.

2.3 Boundary conditions

Except at the entrance, the same boundary conditions are applied for all simulations. The static pressure P_s is specified at the outlet boundary as the uniform value of zero. In addition, no-slip boundary condition is applied on the walls. To solely study the effect of entrance velocity distributions, the flow rate is set to the value of $Q = \frac{\pi \nu Re D}{8}$ for each inlet condition.

The entrance boundary conditions described below are prescribed to the inlet of the straight section located $3.5D$ upstream of the bend entrance. Four groups of inflow profiles are considered and detailed in following sections, with corresponding presentations in Fig. 2.

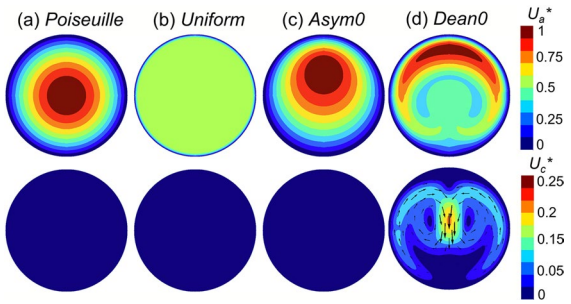

Fig. 2 Entry axial (top) and cross-sectional (bottom) velocities normalized by $2\bar{U}$ distributions at $3.4D$ upstream the curvature entrance: **a** *Poiseuille*, **b** *Uniform*, **c** *Asym0*, **d** *Dean0*. An orientation of 0° about local curvature direction is presented as example. (Reminder: The outer wall of the curvature is located on the top of each section)

2.3.1 Poiseuille and uniform entrance conditions

All radial and azimuthal components of the velocity field are zero at the inflow cross section. For the first entrance condition, denoted *Poiseuille*, the axial velocity component is prescribed using the *coded fixed value* boundary condition in OpenFoam® by:

$$U(M) = 2\bar{U}\left(1 - \frac{r_M^2}{R^2}\right) \tag{1}$$

For the second entrance condition, denoted *Uniform*, all streamwise components are set at mean velocity $\bar{U}$ using *fixed value* in OpenFOAM® $U(M) = \bar{U}$.

2.3.2 Asymmetric-Poiseuille entrance condition

The third entrance condition involves a slightly distorted Poiseuille profile, simulating a laminar flow significantly off-center. As described in Eq. (2) below, an offset vector $\overrightarrow{OC}$ is applied to *Poiseuille* profile, with O representing the center of the inflow section, C denoting the off-center of the distorted profile, M being any point inside the inflow section, and Q_M the intersection of the half-line $[CM)$ with the circumference of the artery model. The inlet condition reads:

$$U(M) = 2\bar{U}\left(1 - \frac{CM^2}{CQ_M^2}\right) \tag{2}$$

Three scenarios are investigated: $\overrightarrow{OC}$ values of $0.25D\mathbf{y}$, $-0.25D\mathbf{y}$ or $0.25D\mathbf{z}$, denoted as *Asym0*, *Asym180* and *Asym90*, corresponding to three different orientations of the entrance flow offset about the vessel curvature: at 0° (anticipating the natural offset generated by the bend), 180° (on the opposite side of the natural offset generated by the bend), and 90° (perpendicular to the bend direction), respectively. This investigation of three scenarios aims to assess the impact of the orientation relative to the vessel curvature under an off-center laminar profile. These entrance conditions are also implemented using *coded fixed value* in OpenFOAM®.

2.3.3 Dean-type entrance condition

Considering the presence of a curved portion upstream the simulated section, the fourth condition is formulated by extrapolating previous velocity field results. Specifically, the implemented entrance velocity distribution is derived from the velocity field obtained at $1.5D$ downstream from the bend exit in our simulations with the *Poiseuille* entrance condition. The verification of flow rate equivalence is automatically ensured.

Similar to the *Asym* condition described above, three cases are explored: 0° (mimicking an upstream tube portion curved in the same direction as the simulated portion), 180° (mimicking an upstream tube portion curved in the opposite direction) and 90° (mimicking an orientation of the inflow pattern perpendicular to the curvature), denoted as *Dean0*, *Dean180* and *Dean90* respectively. In practice, the *time varying mapped fixed value* condition from OpenFOAM® tools is used to extrapolate the velocity field.

2.4 Flow analysis

To enhance the clarity of the flow description, the velocity field is decomposed into axial and cross-sectional components using *coded function object* of OpenFOAM®. Visualization of the contour figures is achieved through the Python library PyVista [40]. WSS vector for each element face along the wall patches is directly computed using the *wall Shear Stress* function object: $\mathbf{R} \cdot \mathbf{n}$, where $\mathbf{n}$ is patch normal vector into the domain, and $\mathbf{R} = \eta(\nabla\mathbf{U} + [\nabla\mathbf{U}]^T)$ the stress tensor for an incompressible flow. The axial component is examined as it is dominant. The axial

WSS values are obtained by: $(\mathbf{R} \cdot \mathbf{n}) \cdot \mathbf{s}$, where $\mathbf{s}$ is the axial direction. In the following section, the velocity and WSS values are normalized by values from a laminar flow in straight pipe:

$$WSS^* = \frac{WSS}{(4\rho\nu\bar{U}/R)} \qquad U^* = \frac{U}{2\bar{U}}$$

3 Results

3.1 Flow description

Four positions along the pipe (illustrated in Fig. 1) are presented to characterize the flow: at the bend entrance $\theta_1 = 0$ ($s = -2.9D$), inside the bend region $\theta_2 = 35°$ ($s = -1.8D$), at the bend exit $\theta_3 = 55°$ ($s = 0$), and $s = 4D$ downstream of the bend. The following sections will present results at $Re = 1100$ for the eight entrance conditions introduced above, at these four positions. As for $Re = 560$, only the maximum values of total WSS are presented in Table 2.

3.1.1 Axial velocity

Figure 3 displays velocity profiles under the six conditions that are symmetric about the y-axis.

(1) When the fluid enters the bend ($\theta_1 = 0$), the flow has undergone a slight deflection towards the inner wall under all conditions. As a result, for the flow conditions that were axisymmetrical at the entrance (cases (a) and (b)), the velocity profiles at $\theta_1 = 0$ exhibit a slight inward asymmetry, while the flows with an initial inward offset ((e) and (f)) present an increased deflection. Meanwhile, the flows with an initial outward offset ((c) and (d)) keep high axial velocities near the outer side.

(2) Downstream the bend entrance, the peak axial velocities start to move towards the outer wall. This change in the flow direction is predicted theoretically by Singh [17], who showed the cross-over effect due to the change of geometry.

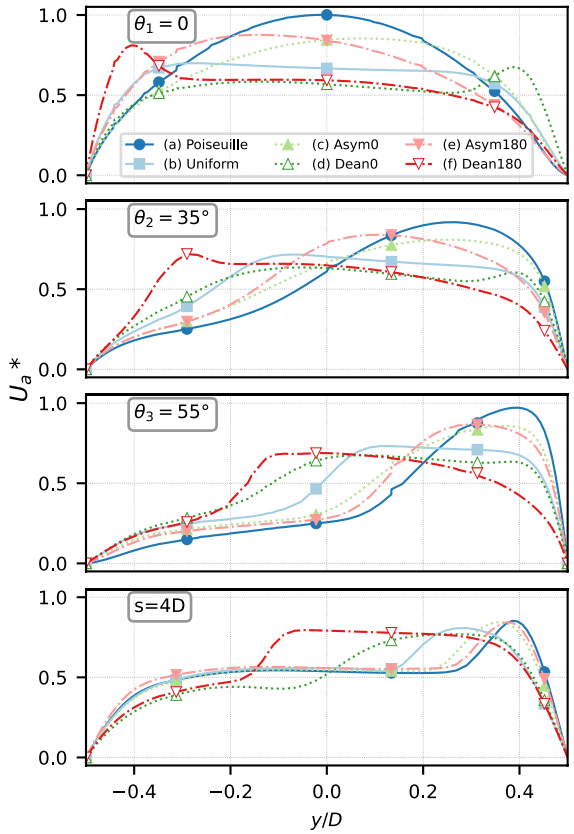

Fig. 3 Normalized axial velocity U_a^* profiles for conditions symmetric about y-axis: **a** *Poiseuille*, **b** *Uniform*, **c** *Asym0*, **d** *Dean0*, **e** *Asym180* **f** *Dean180*. ($y = 0.5D$ is located at the outer wall)

Table 2 Maximum values of total WSS^* magnitude for all conditions (a–h)

Re	Axisymmetry		Plane-symmetry				Non-symmetry	
	Poiseuille	Uniform	Asym0	Dean0	Asym180	Dean180	Asym90	Dean90
560	4.91	3.35	4.24	3.13	4.24	2.90†	4.91*	4.69*
1100	6.02	3.63	4.89	3.30	4.66	3.86†	5.90*	7.05*

Dagger (†) and asterisk (*) denote that the location differs from other values shown in the table. Under the *Dean180* condition, the maximum value occurs at the bend entrance on the inner wall. For the *Dean90* condition, the maximum value is located at 19° and 10° off the y-axis at $Re = 560$ and $Re = 1100$, respectively, while for the *Asym90* case, the maximum is observed at 1° off the y-axis at both *Re*. For the rest, the maximal value occurs at the bend exit on the outer wall

This phenomenon is observed except for the case of *Dean0*, whose peak axial velocity moves outwards since the begining. As the flow progresses along the bend ($\theta_2 = 35°$ to $\theta_3 = 55°$), the boundary layers become thinner near the outer wall and thicker near the inner wall.

(3) When the flow exits the bend ($\theta_3 = 55°$), high axial velocities are observed near the outer wall, except for the *Dean180* condition (f), which retains history of its entrance structure. The *Poiseuille* condition gives the maximum peak velocity and its skewness towards the outer wall is the most pronounced.

(4) The more the flow advances downstream the bend ($s = 4D$), the more the profiles flatten in the core, except for the *Dean180* condition (f) where a high velocity plateau till the core is observed. However, the velocity profiles tend progressively to become similar to each other, with an intense outward skewness which is characterized by a thin boundary layer.

Figure 4 presents the axial velocity contours of the last two conditions, which are not symmetrical with respect of y-axis, with an angle of 90° between the inflow plane and the curvature plane. In the *Asym90* case, the bend imposes the outward deviation of the flow ($\theta_2 = 35°$). The *Dean90* condition generates a more complex flow structure in the bend. However, a similar result for both is observed downstream the bend ($s = 4D$), with a more pronounced twisted structure for the *Dean90* case.

3.1.2 Cross-sectional velocity

Figure 5 displays contour plots of the cross-sectional velocity at the four positions of interest. Near the bend entrance, the velocity vectors point globally inwards for all conditions except for the *Dean0* case (d), which exhibits velocity vectors outwards in the core, in accordance with the flow structure imposed at the pipe entrance. Inside the bend, a pair of counter-rotating vortices is observed for all entrance conditions, the velocity vectors pointing continually inwards along the lateral walls, but outwards in the core. The cross-sectional velocity reaches the strongest values before the bend exit ($\theta_3 = 55°$), before the change of geometry at the bend exit.

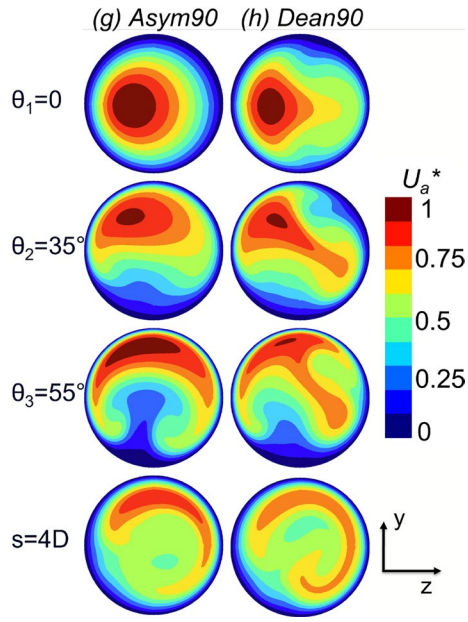

Fig. 4 Normalized axial velocity U_a^* contours for conditions non-symmetric about y-axis: **g** *Asym90*, **h** *Dean90*. (Reminder: The outer wall of the curvature is located on the top of each section)

The secondary flow motion gradually diminishes downstream, while the high velocity vectors persistently point outwards.

3.2 Wall shear stress

The axial component is examined as it is the main one. The axial WSS distributions along the pipe, on the outer side ($y = \frac{D}{2}$) and inner side ($y = -\frac{D}{2}$) are depicted in Fig. 6a, b respectively.

For all conditions, a peak in WSS occurs at the bend exit along the outer wall (Fig. 6a). The highest axial WSS value is observed under the *Dean90* condition (h), followed by the *Poiseuille* condition. The *Dean90* case yields also the highest WSS gradient, followed by the *Poiseuille* condition. A peak at the bend entrance along the inner wall is also observed (Fig. 6b). The highest value is observed for the case *Dean180*, for which the flow structure imposed at the pipe entrance (at $s = -6.3D$) already generates high WSS on the inner wall upstream the bend entrance. In the other cases, this WSS peak remains lower than the one at the bend exit on the outer wall. The WSS distribution for the *Asym* conditions differs only slightly

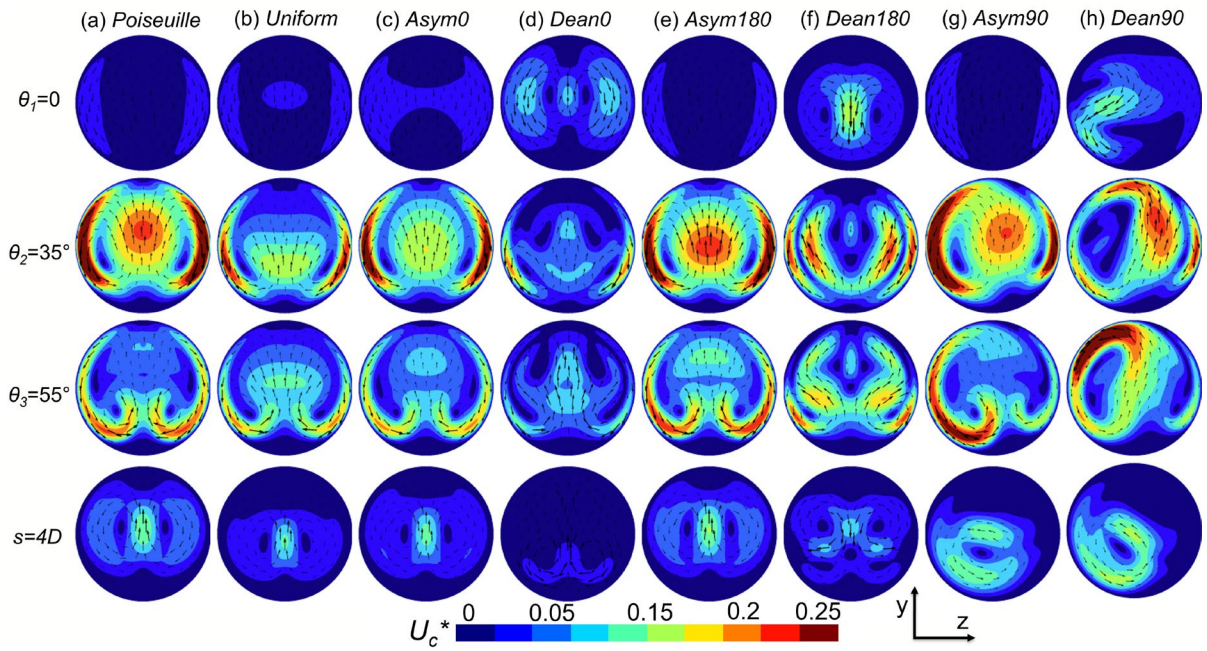

Fig. 5 Normalized cross-sectional velocity U_c^* contours and vector maps, for the eight entrance conditions (a–h) and at four positions along the pipe; ($\theta = 0°$, 35°, 55° and $4D$ upstream). (Reminder: The outer wall of the curvature is located on the top of each section)

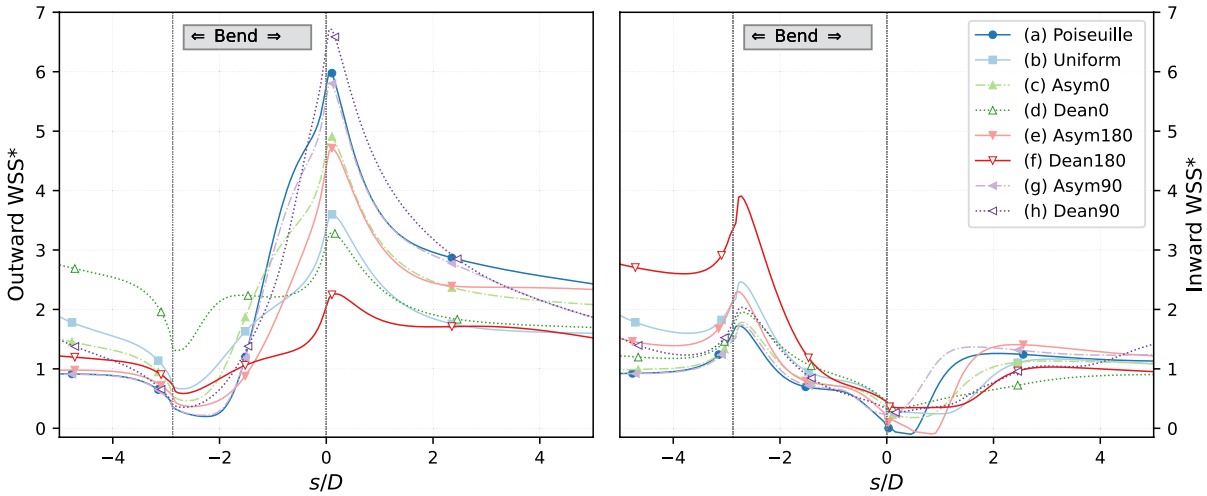

Fig. 6 Normalized axial wall shear stress WSS^* profiles under varied conditions (a–h), for $Re = 1100$. On the left: profile along the outer side, and on the right: profile along the inner side. These profiles span the centerline from $s = -5D$ to $s = 5D$. The x-abscissa of both profiles represents the curvilinear abscissa s along the pipe centerline

from the *Poiseuille* condition, especially when the entrance flow offset is perpendicular to the bend direction (*Asym90*). The most distinguishable case is the *Asym180*, with difference of 2% at the bend entrance and 19% at the bend exit relative to the *Poiseuille* values.

The maximum values of total WSS for all conditions (a–h) are shown in Table 2. Specifically,

configurations (a) to (f) exhibit symmetry about the vertical plane containing the entire centerline of the pipe. Consequently, the flow also possesses the same plane symmetry, and the maximum of WSS is localized on this plane. For all these plane-symmetrical conditions (a–f), the extreme sites are located at the bend exit on the outer wall, except under the *Asym180* condition, where the maximum value occurs at the bend entrance on the inner side. These maximal values are marked with a † sign in Table 2 to remind that they are achieved at the bend entrance. Concerning the two non plane-symmetrical configurations (g–h), the location of maximal WSS is slightly shifted from the outer line ($y = \frac{D}{2}$) due to the twisting in the flow structure, as shown in the WSS^* contour map (Fig. 7). For the *Asym90* condition (g), the maximal WSS value does not differ much from *Poiseuille* inlet, while the *Dean90* case (h) provides a WSS maximum 20% higher than *Poiseuille* at $Re = 1100$. The corresponding values are labeled by a * sign in Table 2. While at $Re = 560$, the *Poiseuille* entry condition generates the maximal value.

4 Discussion

The objective of this work was to examine the impact of entrance conditions on WSS distribution in a curved vessel mimicking a human EIA flow under resting and moderate exercise conditions. Previous studies have focused on the effect of entry conditions on *low* WSS distribution, in association with atherosclerotic plaque development. In contrast, the present study focuses on the effect of entry conditions on *high* WSS distribution, in relation to the development of non-atherosclerotic plaque. Under all entry conditions investigated, when the flow enters the bend, the fluid deflects towards the outer wall due to the centrifugal force, diminishing the thickness of the outward boundary layer as seen in Figs. 3 and 4, increasing the axial component of WSS. Inside the bend, the cross-sectional Dean-type flow is formed as shown in Fig. 5, which creates circumferential velocity gradients at the wall, leading to a circumferential component of WSS. However the cross-sectional velocity remains approximately four times smaller than the axial one. In the present flow configuration, the WSS is dominated by its axial component, which is consistent with Gammack's work for a loosely curved pipe [41]. Entrance conditions influence the formation of cross-sectional structures, directly impacting the position of peak axial velocity in relation to the boundary layer thickness and subsequently the location of high WSS.

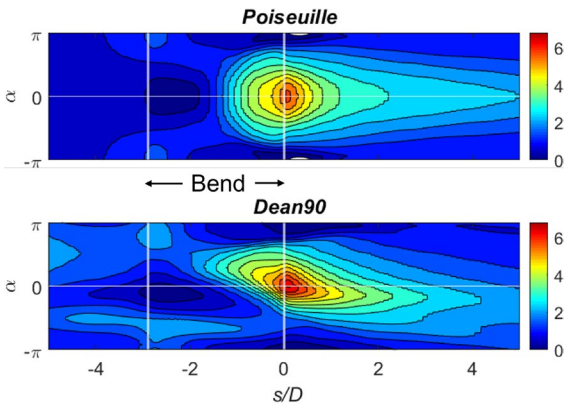

Fig. 7 Normalised WSS^* contour map of the unfolded curved pipe surface under *Poiseuille* (top) and *Dean90* (bottom) entry conditions, for $Re = 1100$. From $s = -5D$ to $s = 5D$ in the axial direction and $-\pi$ to π in the circumferential direction. The outer wall of the curvature is located at circumferential angle $\alpha = 0$ and the inner wall at $\alpha = \pm\pi$

Generally in the present study, higher WSS are observed on the outer wall and lower WSS along the inner wall. This finding is consistent with the results reported by Kirpalani *et al.* in the right coronary artery for experimental results under steady flow at Reynolds numbers of 500 and 1000 [42]. A sharp maximal value is observed at the bend exit on the outer wall. The presence of a WSS peak along the outer wall coincides with the recent histological study on EIAE showing that the artery damage occurs predominantly along the outer bend of the vessels [14]. This coincidence is in favor of the etiological link established between the exaggerated WSS and the endofibrotic plaque development [11–13].

While the entry condition significantly affects the maximum WSS value, it remains within the same order of magnitude. At $Re = 560$, the highest WSS value is given by the *Poiseuille* condition and reaches 4.9 times the value of the laminar straight flow. At $Re = 1100$, the maximum generated by the *Dean90* entrance condition reaches 6 times the value of the laminar straight flow, 17% higher than the value for the *Poiseuille* case. Considering the small difference, opting for *Poiseuille* profile as the entry condition for

further studies of human EIA flow would be a good choice since it is representative of a very generic situation while giving good evaluations of maximum WSS values reached in any configuration.

4.1 Influence of entry conditions along the pipe

Before the bend entrance ($s < -2.9D$), for entry conditions different from the *Poiseuille* case, due to the lack of flow development in the straight section upstream of the bend, WSS values are higher (Fig. 6, curves (b) to (h)) compared to the fully developed *Poiseuille* flow condition (Fig. 6, curves (a)). This result is consistent with other studies that have compared the effect of *Poiseuille* and uniform inlet velocity profiles on WSS distribution [3, 20].

In the bend entrance region, due to the cross-sectional inward flow motion observed for all entry conditions except the *Dean0* case (Fig. 5 ($\theta_1 = 0$)), the peak axial velocity is displaced towards the inner wall, resulting in a peak on the inward WSS at the bend entrance. As expected, the *Dean180* condition exhibits the highest inward WSS due to the flow structure injected at the pipe inlet which already presents a high-velocity offset towards the inner wall.

Inside the bend, the Dean eddy structure is formed: along the lateral walls the cross-sectional velocity vectors point continually inwards, but outwards in the core.

At the bend exit region, for all entry conditions, as the peak axial velocity is pushed further to the outer wall, the boundary layer gradually diminishes at the outer wall, peaking at the bend exit, consequently providing a sharp increase of outward WSS. The Dean eddy structure persists at $4D$ downstream the bend exit.

4.2 Case of Dean-type entrance conditions

Concerning the entrance conditions with Dean-type secondary flow, which are the most realistic conditions mimicking an upstream curved pipe, the highest WSS is observed for the case of orientation offset perpendicular with bend direction (*Dean90*). In this case, the WSS peak position deviates from the y-axis, but only slightly, with less than 20° off-axis at the flow conditions considered, as shown in the WSS^* contour map (Fig. 7).

As another exception, *Dean180* is the only entry condition whose maximum WSS is reached at the bend entrance. It generates 69% and 126% higher inward WSS at Re=560 and Re=1100 respectively comparing to the *Poiseuille* case.

For the *Dean0* condition, a significant zone of stagnation of cross-sectional flow is observed on the outer wall inside the bend, thereby reducing the outward displacement of axial velocity, resulting in a less increased outward WSS. As a result, the flow structure generated in the bend is not amplified by an inlet flow structure in the same direction, contrary to what might have been expected. Moreover, producing the smallest cross-sectional flow motion, *Dean0* generates the most uniform WSS distribution, in contrast to Caro et al.'s suggestion that enhanced in-plane mixing leads to a more uniform WSS distribution in their vascular prostheses study [43].

5 Conclusion

This work explores the influence of entrance conditions on WSS distribution in a curved pipe flow of human EIA model, with a particular emphasis on the maximum values of WSS and their locations. For the examined entrance conditions, a sharp maximum of WSS is consistently located at the bend exit on the outer wall. When compared to recent histological results on EIAE, this location tends to confirm the link established between the exaggerated WSS and the endofibrosic plaque development. While the entry condition significantly affects the maximum WSS value, this value remains within the same order of magnitude. This implies that selecting *Poiseuille* flow as the entry condition to capture extreme WSS values in EIA flow would be a good choice for further studies on EIAE.

The role of entrance conditions in steady EIA flows has been studied as a preliminary approach: incorporating additional flow conditions encountered by athletes in endurance sports is necessary for a more comprehensive understanding of EIAE, and further studies should explore the influence of the EIA's curvature radius and angular aperture on WSS distribution, offering significant insights into

the interplay between vessel geometry and hemodynamic characteristics.

Acknowledgements This work was supported by LabEx CeLyA (ANR-10-LABX-0060) and Partenariats Hubert Curien (PHC Utique 22G1107).

Availability of data and materials The data that support the findings of this study are available from the corresponding author, upon reasonable request.

Declarations

Ethics approval This article does not present research with ethical considerations.

References

1. Hirsch AT, Haskal ZJ, Hertzer NR, Bakal CW, Creager MA, Halperin JL et al (2006) ACC/AHA 2005 practice guidelines for the management of patients with peripheral arterial disease (lower extremity, renal, mesenteric, and abdominal Aortic). Circulation 113(11):e463–e654. https://doi.org/10.1161/CIRCULATIONAHA.106.174526
2. Ku DN, Giddens DP, Zarins CK, Glagov S (1985) Pulsatile flow and atherosclerosis in the human carotid bifurcation. positive correlation between plaque location and low oscillating shear stress. Arterioscler: Off J Am Heart Assoc Inc 5(3):293–302. https://doi.org/10.1161/01.ATV.5.3.293
3. Myers JG, Moore JA, Ojha M, Johnston KW, Ethier CR (2001) Factors influencing blood flow patterns in the human right coronary artery. Ann Biomed Eng 29(2):109–120. https://doi.org/10.1114/1.1349703
4. Caro CG, Fitz-Gerald JM, Schroter RC (1969) Arterial wall shear and distribution of early atheroma in man. Nature 223(5211):1159–1161. https://doi.org/10.1038/2231159a0
5. Shaaban AM, Duerinckx AJ (2000) Wall shear stress and early atherosclerosis. Am J Roentgenol 174(6):1657–1665. https://doi.org/10.2214/ajr.174.6.1741657
6. Tarbell JM, Shi ZD, Dunn J, Jo H (2014) Fluid mechanics, arterial disease, and gene expression. Annu Rev Fluid Mech 46(1):591–614. https://doi.org/10.1146/annurev-fluid-010313-141309
7. Kawarada O (2017) Nonatherosclerotic Peripheral Artery Disease. In: Angiography and Endovascular Therapy for Peripheral Artery Disease. IntechOpen
8. Weinberg I, Jaff MR (2012) Nonatherosclerotic arterial disorders of the lower extremities. Circulation 126(2):213–222. https://doi.org/10.1161/CIRCULATIONAHA.111.060335
9. Dolan JM, Kolega J, Meng H (2013) High wall shear stress and spatial gradients in vascular pathology: a review. Ann Biomed Eng 41(7):1411–1427. https://doi.org/10.1007/s10439-012-0695-0
10. Chevalier JM, Enon B, Walder J, Barral X, Pillet J, Megret A et al (1986) Endofibrosis of the external iliac artery in bicycle racers: an unrecognized pathological state. Ann Vasc Surg 1(3):297–303. https://doi.org/10.1016/S0890-5096(06)60123-4
11. Mosimann R, Walder J, Van Melle G (1985) Stenotic intimal thickening of the external iliac artery: illness of the competition cyclists? report of two cases. Vasc Surg 19(4):258–263. https://doi.org/10.1177/153857448501900411
12. Abraham P, Feugier P (2021) Endofibrose iliaque externe. Archives des Maladies du Coeur et des Vaisseaux - Pratique 2021(303):8–13. https://doi.org/10.1016/j.amcp.2021.10.004
13. Kral CA, Han DC, Edwards WD, Spittell PC, Tazelaar HD, Cherry KJ (2002) Obstructive external iliac arteriopathy in avid bicyclists: new and variable histopathologic features in four women. J Vasc Surg 36(3):565–570. https://doi.org/10.1067/mva.2002.126558
14. Pauline B (2020) Caracterisation Anatomopathologique Des Lesions d Endofibrose Arterielle Etude Comparative Sur Une Serie de 130 Cas
15. Feugier P, Chevalier JM (2004) Endofibrosis of the iliac arteries: an underestimated problem. Acta Chir Belg 104(6):635–640. https://doi.org/10.1080/00015458.2004.11679635
16. Berger SA, Talbot L, Yao LS (1983) Flow in curved pipes. Annu Rev Fluid Mech 15(1):461–512. https://doi.org/10.1146/annurev.fl.15.010183.002333
17. Singh MP (1974) Entry flow in a curved pipe. J Fluid Mech 65(3):517–539. https://doi.org/10.1017/S0022112074001522
18. Agrawal Y, Talbot L, Gong K (1978) Laser anemometer study of flow development in curved circular pipes. J Fluid Mech 85(3):497–518. https://doi.org/10.1017/S0022112078000762
19. Yeung WS (1980) Laminar boundary-layer flow near the entry of a curved circular pipe. J Appl Mech 47(4):697–702. https://doi.org/10.1115/1.3153776
20. Cox C, Plesniak MW (2021) The effect of entrance flow development on vortex formation and wall shear stress in a curved artery model. Phys Fluids 33(10):101908. https://doi.org/10.1063/5.0062565
21. Ito H (1987) Flow in curved pipes. JSME Int J 30(262):543–552. https://doi.org/10.1299/jsme1987.30.543
22. Yao LS, Berger SA (1975) Entry flow in a curved pipe. J Fluid Mech 67(1):177–196. https://doi.org/10.1017/S0022112075000237
23. Williams GS, Hubbell CW, Fenkell GH (1902) Experiments at Detroit, Mich., on the effect of curvature upon the flow of water in pipes. Trans Am Soc Civ Eng 47(1):1–196. https://doi.org/10.1061/TACEAT.0001496
24. Dean MR (1927) Note on the motion of fluid in a curved pipe. The London, Edinburgh, and Dublin Philos Mag J Sci 4(20):208–223. https://doi.org/10.1080/14786440708564324
25. McConalogue DJ, Srivastava RS, Lighthill MJ (1997) Motion of a fluid in a curved tube. Proc R Soc Lond A 307(1488):37–53. https://doi.org/10.1098/rspa.1968.0173

26. Ku DN, Glagov S, Moore JE, Zarins CK (1989) Flow patterns in the abdominal aorta under simulated postprandial and exercise conditions: an experimental study. J Vasc Surg 9(2):309–316. https://doi.org/10.1016/0741-5214(89)90051-7
27. Eustice J, Larmor J (1997) Flow of water in curved pipes. Proc Royal Soc London Ser A, Contain Papers Math Phys Charact 84(568):107–118. https://doi.org/10.1098/rspa.1910.0061
28. Alastruey J, Siggers JH, Peiffer V, Doorly DJ, Sherwin SJ (2012) Reducing the data: analysis of the role of vascular geometry on blood flow patterns in curved vessels. Phys Fluids 24(3):031902. https://doi.org/10.1063/1.3694526
29. Zhang Z, Kleinstreuer C, Kim CS (2001) Effects of curved inlet tubes on air flow and particle deposition in bifurcating lung models. J Biomech 34(5):659–669. https://doi.org/10.1016/S0021-9290(00)00233-5
30. Kováts P, Martins FJWA, Mansour M, Mansour M, Zähringer K, Thévenin D et al (2020) Tomographic PIV measurements and RANS simulations of secondary flows inside a horizontally positioned helically coiled tube. Exp Fluids. https://doi.org/10.1007/s00348-020-02950-6
31. Najjari MR, Plesniak MW (2018) Secondary flow vortical structures in a 180 elastic curved vessel with torsion under steady and pulsatile inflow conditions. Phys Rev Fluids 3. https://doi.org/10.1103/physrevfluids.3.013101
32. Wang H, Ni MJ, Zhang NM (2022) Three-dimensional magnetohydrodynamic flow around a 180° sharp bend under transverse magnetic field. Physics of Fluids. https://doi.org/10.1063/5.0079163
33. Najjari MR, Najjari MR, Cox C, Plesniak MW, Plesniak MW (2019) Formation and interaction of multiple secondary flow vortical structures in a curved pipe: transient and oscillatory flows. J Fluid Mech. https://doi.org/10.1017/jfm.2019.510
34. Caro CG, Dumoulin CL, Graham JMR, Parker KH, Souza SP (1992) Secondary flow in the human common carotid artery imaged by MR angiography. J Biomech Eng 114(1):147–149. https://doi.org/10.1115/1.2895439
35. Galdi G, Robertson A, Rannacher R, Turek S (2008) Hemodynamical Flows: Modeling, Analysis and Simulation
36. Ku DN, Liepsch D (1986) The effects of non-Newtonian viscoelasticity and wall elasticity on flow at a 90° bifurcation. Biorheology 23(4):359–370. https://doi.org/10.3233/BIR-1986-23405
37. Kai Pielhop WS, Klaas Michael (2015) Experimental analysis of the fluid–structure interaction in finite-length straight elastic vessels. Eur J Mech B Fluids. https://doi.org/10.1016/j.euromechflu.2014.11.001
38. Zagzoule M, Khalid-Naciri J, Mauss J (1991) Unsteady wall shear stress in a distensible tube. J Biomech 24(6):435–439. https://doi.org/10.1016/0021-9290(91)90031-H
39. Enayet MM, Gibson MM, Taylor AMKP, Yianneskis M (1982) Laser-Doppler measurements of laminar and turbulent flow in a pipe bend. Int J Heat Fluid Flow 3(4):213–219. https://doi.org/10.1016/0142-727X(82)90024-8
40. Sullivan B, Kaszynski A (2019) PyVista: 3D plotting and mesh analysis through a streamlined interface for the Visualization Toolkit (VTK). J Open Sour Softw 4(37):1450. https://doi.org/10.21105/joss.01450
41. Gammack D, Hydon PE (2001) Flow in pipes with non-uniform curvature and torsion. J Fluid Mech 433:357–382. https://doi.org/10.1017/S0022112001003548
42. Kirpalani A, Park H, Butany J, Johnston KW, Ojha M (1999) Velocity and wall shear stress patterns in the human right coronary artery. J Biomech Eng 121(4):370–375. https://doi.org/10.1115/1.2798333
43. Caro CG, Cheshire NJ, Watkins N (2005) Preliminary comparative study of small amplitude helical and conventional ePTFE arteriovenous shunts in pigs. J R Soc Interface 2(3):261–266. https://doi.org/10.1098/rsif.2005.0044